

RESEARCH ARTICLE

10.1002/2013JB010581

This article is a companion to *Li et al.* [2013] doi:10.1002/jgrb.50358.

Key Points:

- We image Yakutat terrane and Pacific oceanic crust beneath Alaska
- We image a megathrust fault zone with lack of thrust earthquake
- We image the western edge of the Yakutat terrane beneath Kenai Peninsula

Supporting Information:

- Text S1
- Figures S1–S13

Correspondence to:

Y. Kim,
younghkim@snu.ac.kr

Citation:

Kim, Y., G. A. Abers, J. Li, D. Christensen, J. Calkins, and S. Rondenay (2014), Alaska Megathrust 2: Imaging the megathrust zone and Yakutat/Pacific plate interface in the Alaska subduction zone, *J. Geophys. Res. Solid Earth*, 119, doi:10.1002/2013JB010581.

Received 23 AUG 2013

Accepted 1 FEB 2014

Accepted article online 7 FEB 2014

Alaska Megathrust 2: Imaging the megathrust zone and Yakutat/Pacific plate interface in the Alaska subduction zone

YoungHee Kim¹, Geoffrey A. Abers², Jiyao Li^{2,3}, Douglas Christensen⁴, Josh Calkins², and Stéphane Rondenay⁵

¹School of Earth and Environmental Sciences, Seoul National University, Seoul, South Korea, ²Lamont-Doherty Earth Observatory, Columbia University, Palisades, New York, USA, ³Department of Earth and Environmental Sciences, Columbia University, New York, New York, USA, ⁴Geophysical Institute, University of Alaska Fairbanks, Fairbanks, Alaska, USA, ⁵Department of Earth Science, University of Bergen, Bergen, Norway

Abstract We image the slab underneath a 450 km long transect of the Alaska subduction zone to investigate (1) the geometry and velocity structure of the downgoing plate and their relationship to slab seismicity and (2) the interplate coupled zone where the great 1964 earthquake (M_w 9.2) exhibited the largest amount of rupture. The joint teleseismic migration of two array data sets based on receiver functions (RFs) reveals a prominent, shallow-dipping low-velocity layer at ~25–30 km depth in southern Alaska. Modeling of RF amplitudes suggests the existence of a thin layer (V_s of ~2.1–2.6 km/s) that is ~20–40% slower than underlying oceanic crustal velocities, and is sandwiched between the subducted slab and the overriding plate. The observed megathrust layer (with V_p/V_s of 1.9–2.3) may be due to a thick sediment input from the trench in combination with elevated pore fluid pressure in the channel. Our image also includes an unusually thick low-velocity crust subducting with a ~20° dip down to 130 km depth at ~200 km inland beneath central Alaska. The unusual nature of this subducted segment results from the subduction of the Yakutat terrane crust. Our imaged western edge of the Yakutat terrane aligns with the western end of a geodetically locked patch with high slip deficit, and coincides with the boundary of aftershock events from the 1964 earthquake. It appears that this sharp change in the nature of the downgoing plate could control the slip distribution of great earthquakes on this plate interface.

1. Introduction

Material properties of the subduction megathrust greatly influence interplate frictional behavior, such as fault geometry, pore fluids, sediment properties, and mineralogy [Lay et al., 2012, and references therein]. Thus, it is important to constrain such fault zone properties in order to better characterize rupture properties and the extent to which convergent motions between the subducting and the overriding plates are accommodated by earthquake slip, postseismic deformation, and/or interseismic creep in the megathrust environment [Lay and Bilek, 2007]. For example, in Cascadia, the megathrust is characterized as a low-velocity channel following the plate interface downdip into the mantle wedge [Audet et al., 2009; Peacock et al., 2011; Hansen et al., 2012]. High pore fluid pressure is invoked to explain depressed P and S wave velocities and extremely high V_p/V_s ratio above the subducting crust. It is not known if such a seismic structure characterizes other subduction zones.

The Alaska subduction margin exhibits slab dip variability along the Aleutian trench and is seismically active at a range of spatial and temporal scales with segments in different states of the earthquake cycle. In particular, the tectonics of the easternmost part of the margin are complex due to not only subduction of Pacific oceanic lithosphere but also to active terrane accretion since the Mesozoic [Plafker et al., 1994]. Both geophysical and geological evidence suggests subduction of the Yakutat terrane, which is colliding with the North American Plate. Although there have been some efforts to map its geometry offshore, seismic properties of Yakutat terrane have been poorly constrained up-to-date, particularly where it enters the megathrust, where great thrust earthquakes occur.

The shallow subduction dip of the Yakutat slab beneath the Kenai Peninsula has been previously attributed to its anomalously high buoyancy compared to typical oceanic slabs, a result of its elevated crustal thickness

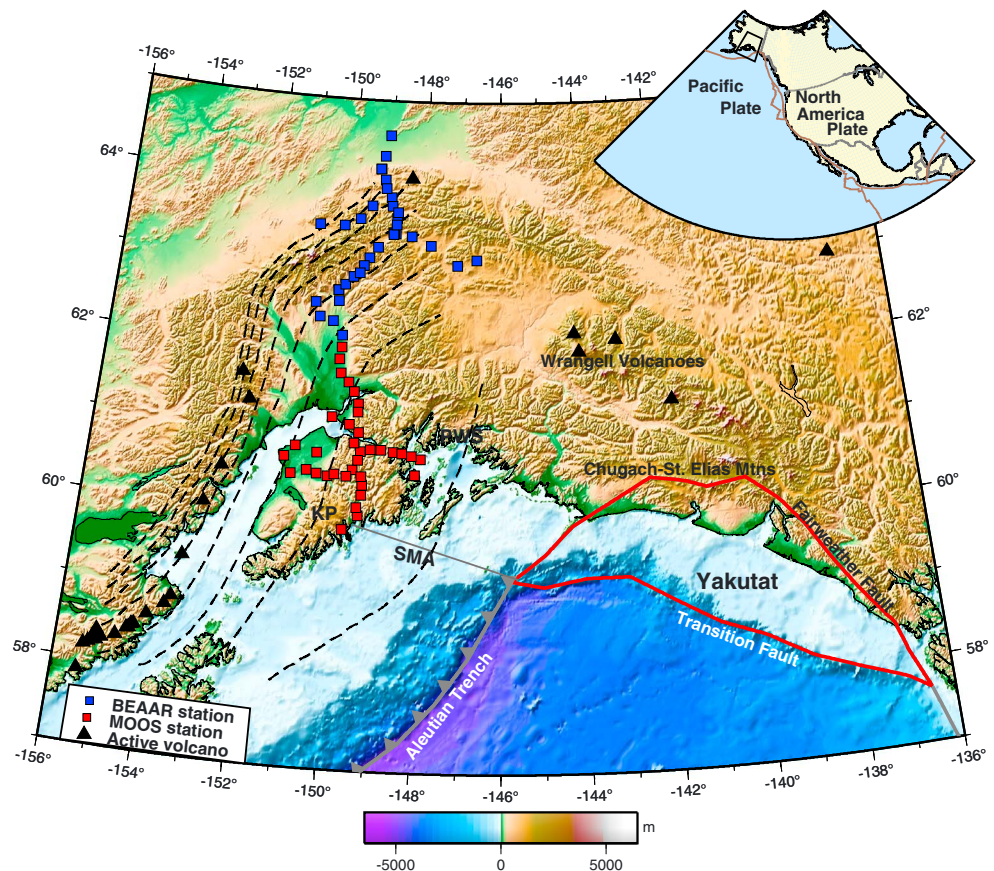


Figure 1. Topographic-bathymetric map showing the region of the study and stations indicated as squares. Inset in the upper-right corner illustrates regional tectonic framework. The black-dashed lines are slab depth contours at 20 km intervals (from 20 km to 160 km) based on Wadati-Benioff seismicity [Li *et al.*, 2013]. The Yakutat terrane boundary is taken from Worthington *et al.* [2012], and the Slope Magnetic Anomaly (SMA) is from Bruns [1983]. KP, Kenai Peninsula; PWS, Prince William Sound.

[Gutscher *et al.*, 2000; Abers, 2008]. Direct evidence comes from a teleseismic receiver function image that shows an unusual overthickened low-velocity crust with a $\sim 25^\circ$ dip that is subducting beneath central Alaska from 70 to ~ 130 km depth [Ferris *et al.*, 2003]. In addition to this seismic image, GPS observations from the dense geodetic network in Alaska [Freymueller *et al.*, 2008; Elliott *et al.*, 2013] and offshore refraction data east of the Kenai Peninsula [Brocher *et al.*, 1994; Fuis *et al.*, 2008; Worthington *et al.*, 2012] support the subduction of the Yakutat terrane. The collision of the Yakutat terrane with the North America plate has been suggested to control the volcanism, mountain building [Plafker *et al.*, 1994], and interplate coupling, and may bound the largest asperity of the 1964 Alaska earthquake [Zweck *et al.*, 2002]. However, there are several aspects of the Pacific-Yakutat slab in southern Alaska that are still poorly known: (1) the geometry and velocity structure of the downgoing plate, in particular, their relation to slab seismicity and metamorphic evolution; (2) the possible structural controls on the rupture of the great earthquake, and the subduction megathrust properties that provide that control; and (3) the 3-D structure of the subducting Pacific-Yakutat slab beneath the Cook Inlet Basin.

In this study, we image the subducted and overriding plates and the intervening deformation zone in the region between the Alaska coastline and central Alaska. The images are generated using data from the 34 broadband stations of the Multidisciplinary Observations of Subduction (MOOS) and nearby permanent stations following Li *et al.* [2013], in southern Alaska, and the 36 stations of the Broadband Experiment Across the Alaska Range (BEAAR) [Ferris *et al.*, 2003], in central Alaska (Figure 1). This data set is particularly interesting because subsets of the MOOS stations in the eastern Kenai Peninsula cover a part

of the 1964 earthquake's main asperity that is known to be strongly coupled [Zweck *et al.*, 2002], which allows us to examine properties of subduction zone megathrust fault in a critical part of the system. Integration with previous offshore studies [e.g., Brocher *et al.*, 1994] provides a continuous transect of over 700 km from the Aleutian trench to central Alaska. In a companion paper [Li *et al.*, 2013], we analyze seismicity along the thrust zone.

1.1. Tectonic Setting

The tectonics of southern Alaska along the Gulf of Alaska margin are dominated by the collision and subduction of the Yakutat terrane as it moves northwest (N26°W) with respect to the North American Plate at 57 mm/yr, a similar rate to Pacific-North America convergence but slightly more westerly (N19°W) [Elliott *et al.*, 2010] since early Miocene [Plafker *et al.*, 1994]. Based on seismic reflection and refraction data, the Yakutat terrane, located offshore of the Kenai Peninsula, was suggested to be (1) wedge-shaped, with crustal thickness increasing west to east from ~15 km to ~30 km [Worthington *et al.*, 2012], and (2) bounded by the Fairweather transform fault to the east, and by the Slope Magnetic Anomaly to the northwest and the Transition Fault to the south [Fuis *et al.*, 2008]. Based on geodetic observations, Elliott *et al.* [2010] suggested ~7.9 mm/yr of convergence across the Transition Fault at its southern boundary and showed that the eastern edge of the Yakutat Block is currently deforming.

The geometry and composition of the subducted Yakutat terrane beneath the Kenai Peninsula are poorly defined from existing imaging. Seismic tomography from regional seismicity roughly delineates the subducted portion of the Yakutat terrane as a thick low-velocity, high V_p/V_s region [Ferris *et al.*, 2003; Eberhart-Phillips *et al.*, 2006]. In central Alaska, seismic images based on teleseismic migration and receiver functions from a dense temporary array (BEAAR; Figures 1 and 2a) showed the thick (11–22 km) crust of the subducted Yakutat terrane and Pacific Plate down to 130 km depth [Ferris *et al.*, 2003; Rondenay *et al.*, 2008, 2010]. The truncation of intermediate-depth seismicity east of 147°W suggests a sharp slab contortion or tear between this location and the Wrangell volcanoes, speculatively both related to absence of Yakutat terrane subduction farther east [Fuis *et al.*, 2008]. Alternatively, the slab may continue east aseismically [Creager and Boyd, 1991], as hinted by low-frequency S receiver functions east of Prince William Sound. The western edge of the subducted terrane lies beneath the Prince William Sound and perhaps the eastern Kenai Peninsula and overlaps with the area of major moment release in the 1964 Alaska earthquake [Christensen and Beck, 1994].

The subducted Yakutat terrane coincides with the eastern part of the 1964 earthquake rupture area and may play an important role in the earthquake's rupture process and the asperity distribution. The GPS vectors suggest a drastic change in plate coupling [Suito and Freymueller, 2009] that occurs in close proximity to the assumed Yakutat/Pacific boundary, but such change in coupling has not been directly constrained. On the western Kenai Peninsula, the southeast-trending geodetic displacement vectors mainly reflect postseismic deformation from the 1964 earthquake, whereas in the east the segment is locked and building stress for the next event [Zweck *et al.*, 2002; Freymueller *et al.*, 2008]. GPS measurements show that the large locked patch beneath the eastern Kenai Peninsula and Prince William Sound extends to a depth of ~30 km, with a slip maximum at ~20 km [Suito and Freymueller, 2009].

1.2. Yakutat Terrane Structure

The Alaskan subduction margin subducts extensive sediment in places, with segments showing tectonic erosion nearby [von Huene *et al.*, 1998; von Huene and Weinrebe, 2012]. In addition to large sediment contribution of its overlying cover, the Yakutat terrane is both subducting and in part accreting onto the North America plate [Bruhn *et al.*, 2004]. In particular, deformation features along the northern boundary of the subducted terrane are suggested to be a combination of accretion of overlying sediments to North America and subduction of the underlying, more mafic crust into the subduction system [Bruhn *et al.*, 2004; Worthington *et al.*, 2012]. Seismic velocities of the sedimentary layer increase toward the shore due to increased sediment compaction and fluid expulsion as the Yakutat terrane impinges on the North American continent [Worthington *et al.*, 2012].

Previous seismic refraction and reflection data (e.g., from Trans-Alaska Crustal Transect (TACT) and St. Elias Erosion and Tectonics Project (STEEP)) provide information regarding the velocity structure,

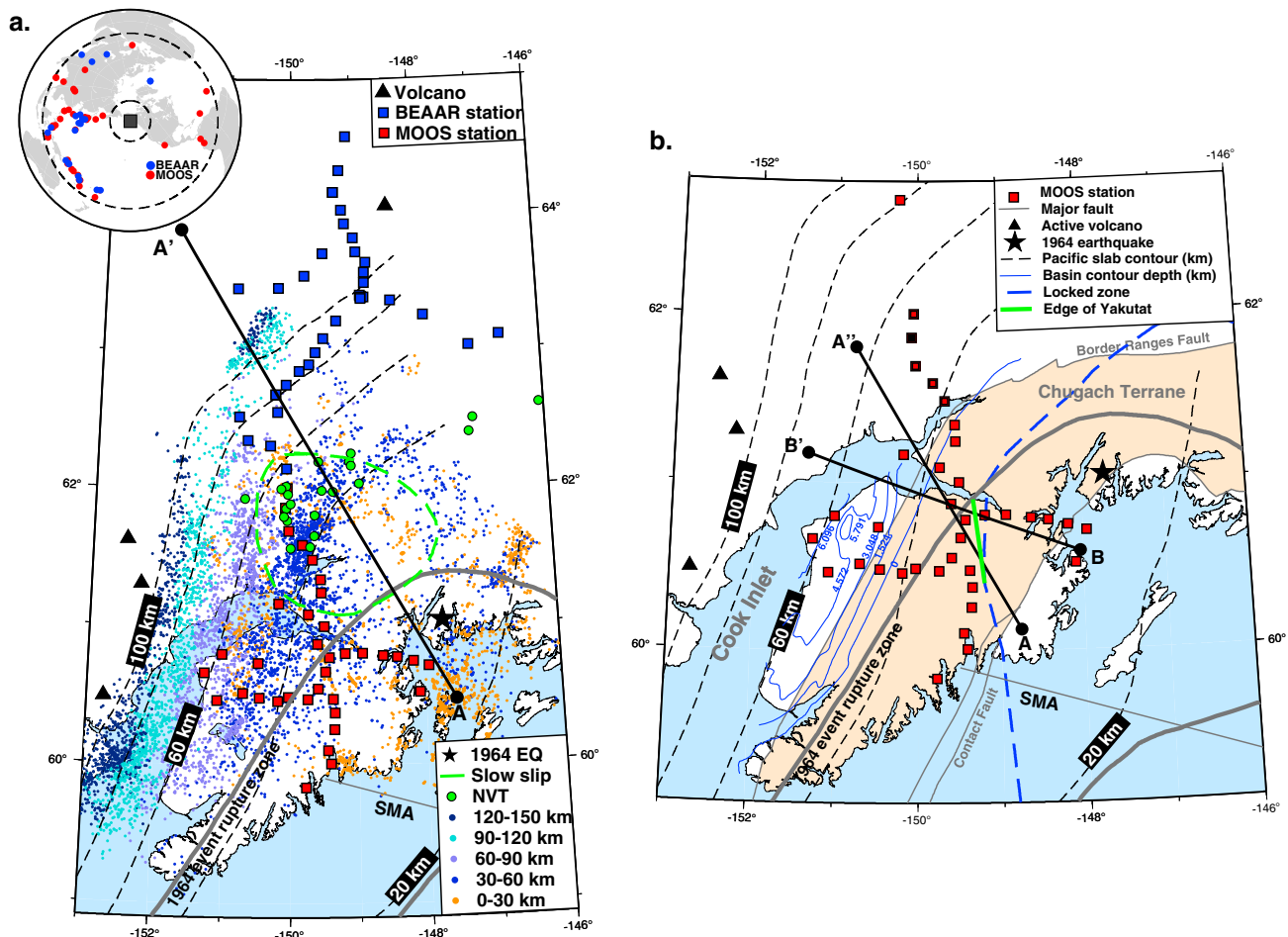


Figure 2. Location map showing seismic stations, relocated seismicity, and major tectonic features in Alaska. (a) Map showing MOOS and BEAAR stations, relocated seismicity from the MOOS [Li et al., 2013], nonvolcanic tremors [Peterson and Christensen, 2009], slow-slip region [Ohta et al., 2006], and the boundary of aftershocks from the 1964 earthquake [Furumoto, 1964; Sykes, 1971]. The inset shows teleseismic earthquake locations used in the migration (MOOS, 40 events: red; BEAAR, 23 events: blue). (b) Regional map showing MOOS stations (red squares), depth contours of the top interface of Pacific oceanic crust (black-dashed lines) [Li et al., 2013], the bottom interface of the Cook Inlet Basin (blue lines) [Shellenbaum et al., 2010], and approximate boundary of high slip deficits (blue-dashed lines) [Suito and Freymueller, 2009]. The map also includes the location of the western edge of Yakutat terrane constrained from imaging (green line). The Chugach terrane is bounded by Border Ranges Fault and Contact Fault. Note images are formed by projecting the stations on lines (A-A' with the azimuth of N330°E in Figure 2a, and B-B' of N290°E and A-A'' of N330°E in Figure 2b). SMA, Slope Magnetic Anomaly.

thickness, and composition of the Yakutat terrane. Brocher et al. [1994] suggested a model of a composite continental-oceanic terrane combining the Yakutat terrane thrust over Pacific oceanic crust of ~15 km thickness beneath Prince William Sound. One feature that was imaged in their study is a ~4 km thick, ~4° dipping layer with the P wave velocity of 6.9 km/s at depths 15–20 km, representing the Yakutat terrane which sits below the megathrust, separated from deeper Pacific crust by a low-velocity sediment layer. However, more recent STEEP refraction data do not show this layering. Christeson et al. [2010, 2013] and Worthington et al. [2012] suggested that there is no evidence for underthrusting of the Pacific oceanic crust beneath the unsubducted Yakutat terrane, but instead, a relatively uniform-velocity thickened mafic crust, with V_p increasing from 6.5 to 7.2 km/s in the middle-lower crust. These velocities and structural relations across the Transition Fault zone led to an interpretation of the Yakutat terrane as an oceanic plateau [Christeson et al., 2010; Worthington et al., 2012]. Furthermore, Christeson et al. [2013] suggested that the average Moho depth of the terrane is ~30 km, but depth increases onshore to 40–45 km beneath the Chugach-St. Elias mountain ranges (Figure 1). Thus, the western Yakutat terrane has been variably interpreted as tectonic doubling of oceanic crust, or an oceanic plateau.

2. Data and Methods

We use two seismic imaging techniques to identify the location and magnitude of seismic discontinuities from scattered waves recorded by a dense array of seismic stations in southern and central Alaska (Figures 1 and 2). Both teleseismic receiver function and higher-resolution teleseismic migration provide images with much more detail on the location of the seismic discontinuities than those previously obtained using more sparse network.

2.1. Teleseismic Migration and Receiver Function

The 2-D generalized radon transform-based migration (hereafter 2-D GRT) method inverts scattered waves within the teleseismic P wave coda for sharp variations in the Earth's elastic properties beneath array stations [Bostock and Rondenay, 1999; Bostock et al., 2001; Rondenay et al., 2005; Rondenay, 2009]. The 2-D GRT method involves two steps: (1) the recorded data are preprocessed to isolate the scattered P and S wavefield from teleseismic P coda [Bostock and Rondenay, 1999] and (2) the 2-D GRT method is applied to produce an image of velocity perturbations. The description of the preprocessing procedure has been fully described in previous papers [Rondenay et al., 2001; MacKenzie et al., 2010; Pearce et al., 2012], and in this study, we follow the preprocessing step improved by Pearce et al. [2012]. The 2-D GRT method is similar to the receiver function (RF) method in that both utilize the converted and scattered teleseismic waves but takes an advantage of array recordings and thus can treat scattering from 2-D structure without the need for simplifying the assumption about the geometry of subsurface structure.

The 2-D GRT method assumes that the scattered wavefield is generated by volumetric perturbations in P and S wave velocities within a smoothly varying background velocity model. The 1-D reference models used in this study are described in section 2.2. The 2-D GRT simultaneously inverts a combination of forward and backscattered (or reverberated) modes using analytical expressions for their travel times and amplitudes. The scattering modes are defined as the incident P wave forward scattered as an S wave (Ps); the free-surface-reflected P wave backscattered as a P wave (PpP); the free-surface-reflected P wave backscattered as an S wave ($PpPs$); and the free-surface-reflected S wave backscattered as an Sv wave ($PpSs|v$) and Sh wave ($PpSs|h$; nomenclature of Zhu and Kanamori [2000]). Only the PpP mode has sensitivity to P wave velocity perturbations (hereafter dV_p/V_p). The four remaining scattering modes are sensitive to S wave velocity perturbations (hereafter dV_s/V_s image) and are combined to form a single composite image using the approach of Rondenay et al. [2001].

We compute the RFs in two ways: (1) stacked radial RFs and (2) stacked RFs after applying a $PpPs$ moveout correction, typically the largest coherent reverberation (see supporting information Figure S1 for a single station). The moveout correction is done to equalize differences in ray parameters in particular phase arrival times, which lead to significant time lag variations for $PpPs$. This allows for direct comparison of RFs for earthquakes from different distances. We choose to perform the $PpPs$ moveout correction instead of Ps moveout because Ps moveout is small so is coherent on stacks with no correction, but the ray parameter variation is large. We use a ray parameter of 0.065 s/km (slowness of 7.0° s^{-1}) as reference. For more details on the RF method, we refer to previously published papers based on the BEAAR data set [Ferris et al., 2003; Rossi et al., 2006], and also array data sets in central Mexico subduction zone [Kim et al., 2010, 2013; Song and Kim, 2012a, 2012b].

2.2. Data

For imaging, the selection of events are based on three criteria [e.g., Pearce et al., 2012]: earthquakes (1) occur within epicentral distances 30 to 90° from the station array, (2) have a magnitude (m_b) greater than 6.0, (3) have an incident P wave arrival that can be identified across the array. Also, we use only a subset of the events with high signal-to-noise ratio, which were recorded at a majority of the stations. The resulting data set from the MOOS array consist of 40 earthquakes that occurred between June 2007 and July 2009 (Figure 2a, inset). For migration, the selected waveforms are bandpass filtered between 0.03 and 0.2 Hz. A similar data selection scheme was previously applied for BEAAR data set [Rondenay et al., 2008, 2010], so we include from that previous study the preprocessed waveforms from 23 events that occurred in 1999–2001 (Figure 2a, inset). We use this merged data to image the structure beneath the continuous transect across different profiles (A-A', A-A'', and B-B') (Figure 2).

Table 1. One-Dimensional Reference Model for a Profile A-A' [Rondenay *et al.*, 2008, 2010]

Layer	Depth Ranges (km)	V_p (km/s)	V_s (km/s)	Density (g/cm ³)
1	0–36.2	6.5	3.7	2.9
2	36.2–300	7.81	4.36	3.4

Seismograms from the five MOOS stations located at the northern end of the MOOS array (Figure 2b, red squares outlined in black line) are noisy due to the near-surface structure, mostly resonances within low-velocity sediments of the

Susitna Basin. We exclude a single station (Figure 2b, black square) in the migration, and the numbers of the preprocessed seismograms from the other noisy stations are much smaller than those from other MOOS stations located in the south. We observe that high-amplitude signals from the noisy stations result in the migration artifacts such as “migration smiles” and continuous ringing.

For RF calculations, less stringent criteria in selecting events are applied than for migration, because the RF modeling is less sensitive to ray aperture and coverage compared to the 2-D GRT method, and stacking of normalized RFs will reduce the high-frequency noise level. Teleseismic waveforms are selected from 66 earthquakes with magnitude greater than 6.0 and the epicentral distances between 30 and 90° away from the MOOS array (supporting information Figure S2). Individual waveform data are (1) time windowed to 90 s, (2) bandpass filtered at 0.01–1.0 Hz, and (3) rotated to radial and tangential coordinates. Radial component seismograms are then deconvolved with vertical component seismograms at each station using time domain iterative deconvolution [Ligorria and Ammon, 1999] with a Gaussian filter parameter of 4.0 (equivalent to 1.92 Hz low-pass filter). We only concentrate on radial RFs in this paper to directly compare the image with the migration images, particularly over the thrust zone where dips are <5°.

3. Seismic Images

Here we present 2-D GRT images and RF images for the Alaska subduction zone system crossing a series of different projection profiles. Both methods constrain depths to major boundaries such as the top of the subducting slab and the oceanic crust/continental crust-mantle interface of the slab, from *P*-*S* mode conversions and reverberations. In migration images, inversions determine the velocity perturbations needed to produce the scattered wavefield [Rondenay *et al.*, 2001, 2005], so the velocity perturbations are shown relative to some unimaged long-wavelength background velocity field (Tables 1 and 2); in general, the data are mostly sensitive to gradients in velocity. Both *P* wave and *S* wave velocities are shown with a red to blue color scale, which represents negative (slower) to positive (faster) velocity perturbations (Figures 3, 4a, 4b, 5a, and 5b). Velocity discontinuities in the migration images are thus denoted by color contrasts (i.e., red-to-blue or blue-to-red) [Rondenay *et al.*, 2005]. For RF backprojections, the amplitude of the conversion is imaged (e.g., Figures 4c and 5c), and the peak of the RF pulse indicates the discontinuity interface with its polarity controlled by the impedance contrast across the discontinuity [Langston, 1979]. We show two sets of images (Figures 4 and 5), one oriented N330°E showing a complete transect of the subduction zone through both arrays, and a shorter cross line oriented N290°E that samples the west edge of the Yakutat terrane beneath the Kenai Peninsula.

3.1. Individual Scattering Modes, Projection Angles, and Background Model

Figure 3 shows composite perturbations and individual mode contributions to dV_s/V_s from forward-scattered (*Ps*) and backscattered phases (*PpPs*, *PpSs|v*, and *PpSs|h*), along with dV_p/V_p from *PpPp*, for the projection azimuth of N330°E along A-A' (Figure 2a), using the 1-D reference model (Table 1). The four scattering modes involving *S* waves (Figures 3b–3e) combine to form the composite dV_s/V_s image used to interpret structure (Figure 3f). We apply different

Table 2. One-Dimensional Reference Model for a Profile B-B' [Li *et al.*, 2013]

Layer	Depth Ranges (km)	V_p (km/s)	V_s (km/s)	Density (g/cm ³)
1	0–15	6.06	3.49	2.71
2	15–30	6.31	3.61	2.79
3	30–45	6.95	3.91	2.99
4	45–70	7.77	4.34	3.26
5	70–110	8.56	4.84	3.51
6	110–300	8.78	4.85	3.58

weight to the four scattering modes (2 for *Ps*, 5 for *PpPs*, 0.5 for *PpSs|v*, and 0.5 for *PpSs|h*) to reduce the contributions from scattering modes that display a weak response [Rondenay *et al.*, 2001]. We show images for each mode contributions for profiles B-B' and A-A' (Figure 2b) in supporting information Figures S3 and S4, respectively.

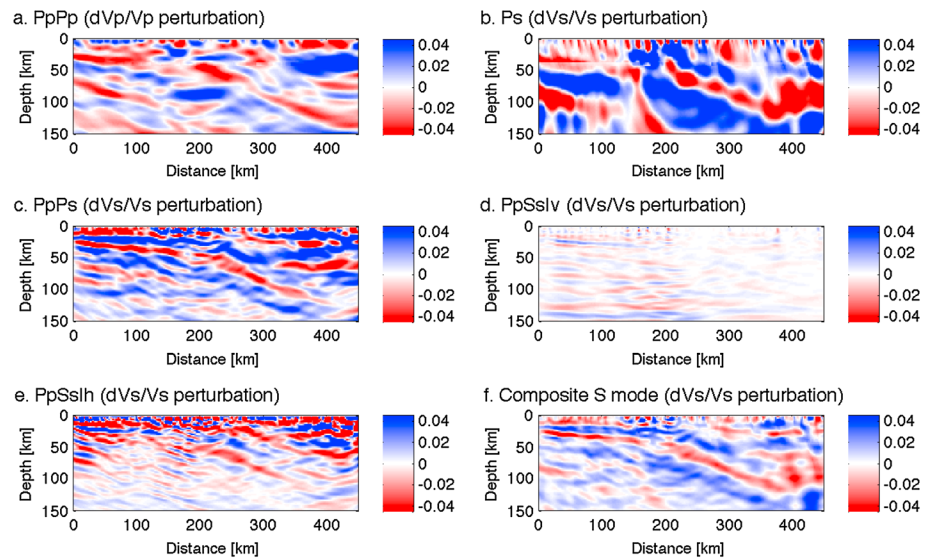


Figure 3. Images showing individual mode contributions. (a–e) Contributions from each scattering modes for one forward (Ps) and four backscattered modes (PpPp, PpPs, PpSslv, and PpSslh), showing the 450 km transect (A–A' in Figure 2a). Red to blue color scale represents negative (slower) to positive (faster) P wave and S wave velocity perturbations relative to the 1-D background model (Table 1). (f) Composite dV_s/V_s image.

On its own, the Ps mode (Figures 3b, S3b, and S4b) does not resolve the thickness of a thin layer (<10 km) due to the lower frequency filter of 0.03–0.2 Hz in the migration. The surface-reflected modes PpPs and PpSs have roughly 3 times better spatial resolution for the same frequencies [e.g., Rondenay, 2009]. As discussed in section 2.2, we exclude noisy station response due to the near-surface structure at the north end of the MOOS array (Figures 2b and 4d) in the migration, to suppress migration artifacts. As shown in Figure 3, the remaining small number of records from the noisy stations does not capture the structure beneath the central array, leaving an apparent hole in the plate boundary (~ 170 to 200 km horizontal coordinate on Ps). Supporting information Figure S5 shows stacked RF trace for the noisy station which was not used in the migration. In addition, the PpSslv mode image does not resolve the structure compared to other seismic modes because all the teleseismic waves are obliquely incident to the seismic array and preferentially excite SH-to-SH backscattering rather than SV backscattering [Rondenay, 2009]; so the PpSslv mode is weak compared to the images from other modes (Figures 3d, S3d, and S4d).

As more migrated individual phases involving S waves are stacked in, we observe that the artifacts due to cross-mode contamination (i.e., parallel echoes of the real structure) [Rondenay, 2009] become attenuated while energy mapped to its correct depth is sharply imaged with increased resolution (Figures 3f, S3f, and S4f). In this paper, we focus on the migrated image obtained from the stack of S scattered waves because it is based on larger number of scattered waves that afford greater volume and dip resolution, and the S scattered waves are more accurately separated from the full wavefield than P waves [Rondenay, 2009]. However, because the P scattering image (Figure 3a) is independent of S scattering, it provides a useful validation of the S scattering image (Figure 3f).

We explore the resolution of migration image from the 2-D GRT method by using a range of projection angles and different background models (see supporting information for details). First, we find that the projection angle of $N330^\circ E \pm 10^\circ$ yields the most focused image of the overall structure along the continuous transect (A–A') beneath both MOOS and BEAAR stations (supporting information Figure S6) and the low-velocity thrust zone along the profile A–A'' beneath MOOS stations only (supporting information Figure S7). We also find that the projection angle of $N290^\circ E \pm 10^\circ$ (B–B') for imaging the Pacific Plate in the west of the array near Cook Inlet (supporting information Figure S8). Second, the same background model is used for both the migration and hypocenter relocation to minimize the source of bias when comparing the location of imaged structures and seismicity. For the profile A–A', we use (1) 1-D velocity model (Table 1) that was previously used in the migration using BEAAR data set [Rondenay et al., 2008, 2010], and (2) 1-D velocity model (Table 2)

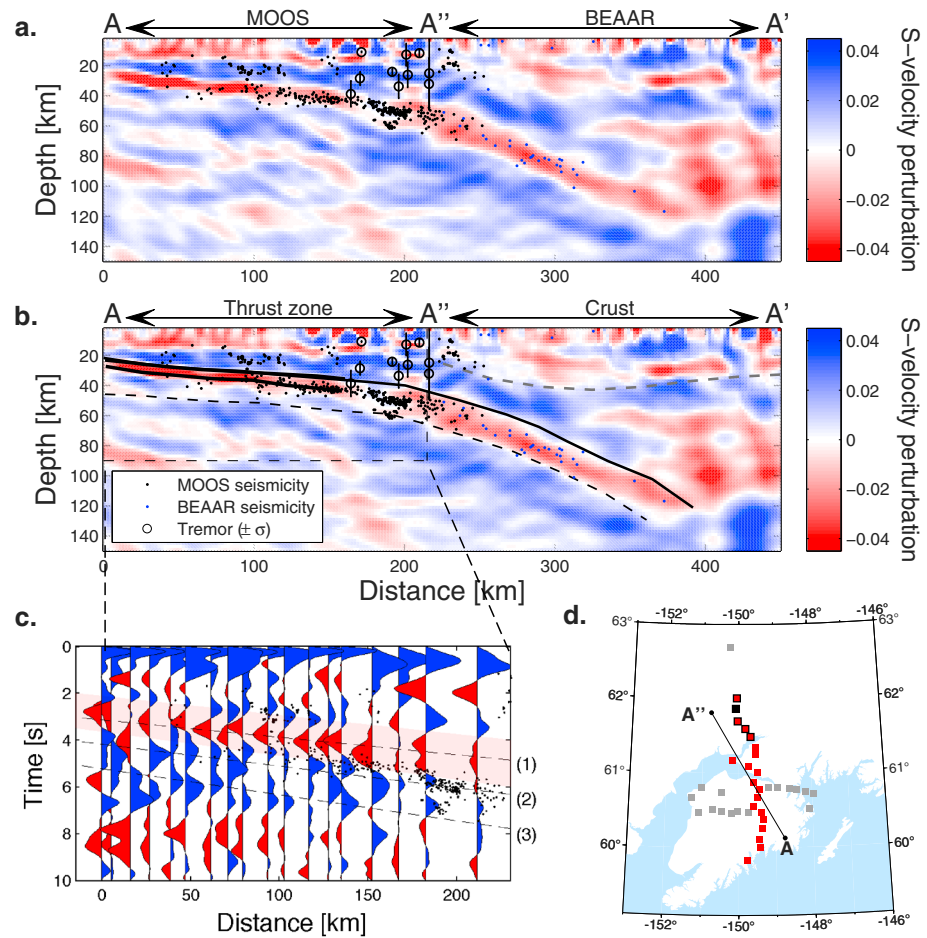


Figure 4. Seismic images along the projection line A-A'. (a) Migrated image using teleseismic earthquakes in all back azimuths (Figure 2a inset) and a subset of MOOS and BEAAR stations (red and blue squares, supporting information Figure S6a). Relocated earthquakes recorded from MOOS [Li et al., 2013] and BEAAR (supporting information Figure S12) [Ferris et al., 2003], and NVTs [Peterson and Christensen, 2009] are also plotted. (b) Interpreted image. The top and bottom interfaces of Yakutat terrane are denoted by black solid line and dashed line, the top and bottom of the thrust zone by thicker lines, and the continental Moho [Rondenay et al., 2010] by gray-dashed line. (c) Stacked RFs along the same projection line (A-A') as migration using earthquakes in all back azimuths (supporting information Figure S2) and a subset of MOOS stations shown in Figure 4d (red squares). Three dashed lines indicate three consistent (negative-positive-positive) pulses ((1)-(2): thrust zone; (3) Yakutat Moho). The negative RF pulse at 2.5–4.5 s is additionally highlighted in pink to indicate that the conversion occurs at the top of the thrust zone and also this oppositely polarized, single pulse waveform gets complicated toward north of the MOOS array (five stations shown squares outlined in black line in Figure 4d, including the black square). Relocated microseismicities from MOOS [Li et al., 2013] are plotted as dots, and their locations mostly coincide with the negative and first positive arrivals. Note that we exclude a single station (KASH, black square) in the migration and RF calculation. (d) Locations of profile A-A' and MOOS array for imaging the thrust zone.

that is consistent with the “Kenai” velocity model used in the relocation of local seismicity recorded from the MOOS array [Li et al., 2013]. For the short profiles B-B' and A-A', we only use the Kenai model (Table 2).

3.2. Migrated dV_s/V_s and RF Images, and Finite-Difference Modeling

3.2.1. Profile A-A': Image of Thrust Zone and Yakutat Terrane

The images (Figure 4) show a thin low-velocity layer with a $<5^\circ$ dip at 20 to 25 km depths near the Alaskan coast (point A) transitioning into a thicker one with a $\sim 20^\circ$ dip at ~ 180 km from the point A (Figure 2a). The velocity perturbations of the thin low-velocity layer (horizontal location = 20–160 km) are estimated to be $dV_p/V_p = -6.8$ to -1.0% and $dV_s/V_s = -7.2$ to -2.0% with the anomaly weakening toward NW, based on the migration images shown in Figures 3a and 3f. The shear velocity reduction estimated from the RFs (Figure 4c) range between $\sim -20\%$ and -40% . The shallower, thin layer corresponds to the interplate thrust zone as

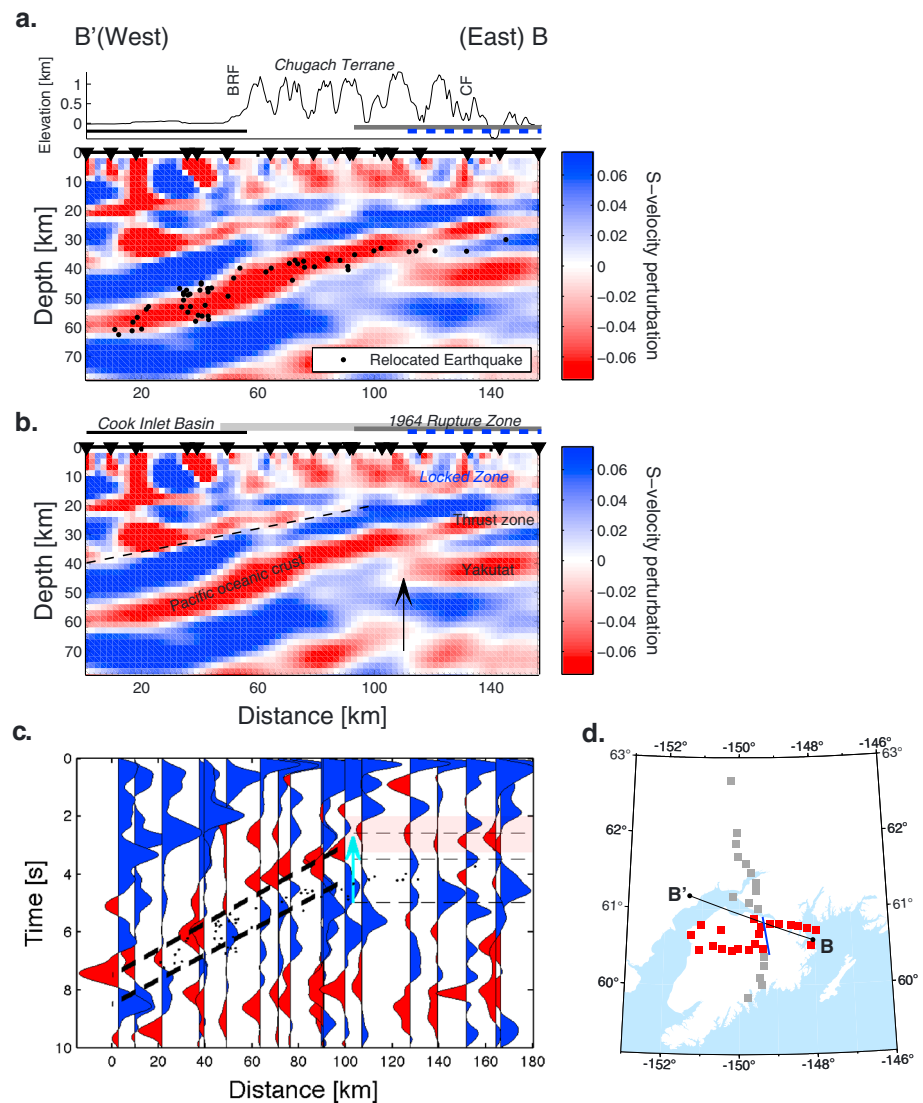


Figure 5. Seismic images along the projection line B-B'. (a) Migrated image (uninterpreted). Black dots represent earthquakes occurring during MOOS experiment and relocated using same velocity model as migration [Li et al., 2013]. Abbreviations shown above the image are BRF, Border Ranges Fault, and CF, Contact Fault. (b) Interpreted image showing low-velocity Pacific oceanic crust, thrust zone, and Yakutat terrane. The black arrow indicates the approximate location showing our image of the western end of the subducted Yakutat terrane. We observe that the western extent of this terrane ends abruptly, 10–15 km east from the western end of the 1964 rupture zone [Furumoto, 1964]. The blue-dashed lines above the images indicate the geotectonically locked zone with high slip deficits [Suito and Freymueller, 2009]. The solid black lines above the images (Figures 5a and 5b) indicate the Cook Inlet Basin [Shellenbaum et al., 2010]. The thin black-dashed line inside the image indicates the bottom of the Contact Fault zone. (c) Stacked RFs along the same projection line (B-B') as migration using earthquakes in all back azimuths (supporting information Figure S2) and a subset of MOOS stations shown in Figure 5d (red squares). Three thin dashed lines indicate three consistent (negative-positive-positive) pulses. The negative RF pulse at 2–3 s is additionally highlighted in pink to indicate that the conversion occurs at the top of the thrust zone. Relocated microseismicity from MOOS [Li et al., 2013] are plotted as dots. The light blue arrow indicates the approximate location of the western end of the Yakutat terrane. Two thick dashed lines indicate locations for the top and bottom of subducting Pacific oceanic crust. (d) Locations of profile and MOOS array, and approximate location of the western end of the Yakutat terrane (blue line).

inferred geotectonically [Freymueller et al., 2008], while the deeper layer has been interpreted previously as subducted crust of Yakutat terrane and Pacific Plate [Ferris et al., 2003; Rondenay et al., 2008, 2010]. The first negative RF pulse (see (1) in Figure 4c) marks the top of the subducted plate or the top interface of the megathrust zone, while the second positive (see (2) in Figure 4c) marks the bottom interface of the megathrust zone, and the last positive (see (3) in Figure 4c) marks arrival in the basement of the subducted

Yakutat terrane. The deeper positive conversion is somewhat clearer on the portion of the cross-line B-B' that lies over the Yakutat terrane (see section 3.2.2 and Figure 5). Most of the relocated seismicity (shown as black dots in Figures 4a and 4b) are within this first low-velocity layer, and the seismicity rate increases toward northwest where the thin layer subsequently thickens by 2–3 km at ~180 km laterally and 40–45 km depth (Figure 4a). As noted by *Li et al.* [2013], all the focal mechanisms within the low-velocity zone show in-plane deformation with downdip *T* axis plunges not thrust faulting; so we infer that the megathrust itself lies at the top of this thin low-velocity zone. Since we use the same velocity model to migrate the images and locate the earthquakes, both are significantly oversampled by the same array of stations (so site effects are similar). Thus, aggregate vertical uncertainty between the image and hypocenter are 1–2 km [*Li et al.*, 2013].

Beneath the north end of the MOOS stations (Figure 4a, horizontal location = 180–200 km), the migrated image depicts the transition from the shallowly dipping structure to steeper structure at greater depth. In this transition, the imaged low-velocity zone appears to be much weaker, but this is likely due to the noisy input signals, which we suppress in the preprocessing step. *Peterson and Christensen* [2009] located nonvolcanic tremor (NVT) that occurred in the region above this dipping thicker crust or at the interface, although their depths have high uncertainty [*Peterson and Christensen*, 2009]. The region also corresponds to the northern extent of a documented slow-slip patch [*Ohta et al.*, 2006].

The clearly imaged, shallowly dipping low-velocity layer can be interpreted as the fault zone based on its relationship with seismicity and geodetic models [e.g., *Suito and Freymueller*, 2009]. It sits at the top of the subducted Yakutat crust, which has higher velocities than the overlying fault zone but lower than those of the subducted oceanic lithosphere. The amplitudes of a deeper low-velocity layer, which might represent the Yakutat crust atop faster mantle, appear to be quite weak and discontinuous (Figure 4a) although the base of the subducted crust is clearly imaged from the RF analysis (see (3) in Figure 4c). We suspect that the very high amplitudes of the overlying fault zone low-velocity layer are masking or damping the Yakutat Moho in these migrations, and also because the slab here dips slightly out of the profile (see section 3.2.2). The full thickness of Yakutat crust can be seen downdip where the fault zone is absent and in B-B' (Figure 2b).

The RF waveforms become broader and complicated toward northwest where the slab is bending more steeply (Figure 4c, horizontal location > 175 km). The amplitude variation may be related to the noisy station response and/or the slab dip. In particular, the 0.5–1.0 s delay in the initial *P* wave arrival from four stations at the northern end of MOOS array (Figures 2b and 4d) represents effects of the sedimentary basin, and strong negative arrivals at 2.0 s lag are likely sediment reverberations. Most of the relocated seismicity [*Li et al.*, 2013] is between the top and bottom of the low-velocity channel imaged in Figure 4a.

In central Alaska, the image of the thick crust subducted beneath the last several MOOS stations and BEAAR stations (beyond ~180 km laterally) fully agrees with previous RF results [*Ferris et al.*, 2003; *Rossi et al.*, 2006] and migration [*Rondenay et al.*, 2008, 2010]. As discussed in *Ferris et al.* [2003], strong *P*-to-*S* conversions are absent below ~130 km depth, as are intraslab earthquakes (Figure 4a). The image of this thick crust gives direct evidence of the exotic terrane subduction in central Alaska [*Ferris et al.*, 2003]. Farther inland in central Alaska (~280 to 450 km laterally in Figure 4a), the upper-plate crustal thickness shallows from 35 km to 25 km toward the north end of the BEAAR array, as terrane boundaries are crossed [*Ferris et al.*, 2003; *Rossi et al.*, 2006; *Veenstra et al.*, 2006; *Rondenay et al.*, 2008, 2010]. We note that there is a difference in the magnitude scale of both *P* and *S* velocity perturbations between this study and previous studies based on the BEAAR data set only [*Rondenay et al.*, 2008, 2010]. The perturbations imaged here are minimum values, a result of incomplete or uneven azimuthal and incidence sampling by sources [*Rondenay*, 2009].

3.2.2. Profile B-B': Image of Subducted Pacific-Yakutat Slab

Figure 5 shows the structure across the Kenai Peninsula beneath the MOOS array. The east end of the line in Prince William Sound includes two low-velocity layers, which end abruptly at horizontal distance of ~110 km from the point B' (Figures 5a–5c). The two low-velocity features are separated by a thin high velocity layer of ~6 km thickness. The top interfaces of the first and second low-velocity layer are at 25 km and ~37 km, respectively. The top low-velocity feature is consistent with the shallowly dipping low-velocity thrust zone imaged across A-A', which is also ~6 km thick (Figure 4a). The bottom low-velocity layer has a thickness of ~15 km, and the western edge is clearly imaged. This bottom low-velocity is not imaged clearly from the profile A-A' (Figure 4a). We note that the main features on this profile are most clearly imaged from the projection azimuth of N290°E ± 10°, roughly perpendicular to Pacific slab strike beneath Cook Inlet

(supporting information Figure S8), which may explain why the lower layer is imaged better here than on A-A'. The transition at the horizontal distance of 110 km corresponds to the western end of the locked patch with high slip deficit [Suito and Freymueller, 2009] and the western end of the 1964 earthquake rupture zone [Furumoto, 1964; Sykes, 1971].

West of the imaged Yakutat edge, the subducted Pacific oceanic crust is clearly imaged as a low-velocity layer, which dips $\sim 25^\circ$ toward northwest beneath Cook Inlet Basin at 30–55 km depth (Figures 5a and 5b), consistent with seismicity [Ratchkovski and Hansen, 2002; Doser and Veilleux, 2009; Li et al., 2013] (see Figures 2b and 5d for approximate location of the edge in a map view). Relocated seismicity from the MOOS array, mostly within the subducted crust, also delineates this subducting layer (Figures 5a and 5c). Both thickness and strength of its low-velocity may appear to be somewhat variable due to nonuniform station spacing and/or noisy station response above the Cook Inlet Basin (Figures 5a and 5b; horizontal location < 60 km). Based on our image, the thickness of the subducted crust is estimated to be 6–8 km, close to the 6.5 ± 0.5 km igneous crust imaged offshore [Brocher et al., 1994] but allowing for some entrainment of subducting sediment. The top of the subducting Pacific crust is 40–55 km deep beneath six stations in the westernmost end of the MOOS array, which cover the eastern portion of the basin.

Above the Pacific crust in the overriding plate, we observe an interface dipping west at 20–40 km depth (Figures 5a and 5b; horizontal location of 10–90 km), which may be the dipping Contact Fault zone, which separates the Chugach terrane from the underlying Prince William Terrane to the southeast [Fuis et al., 2008]. The imaged feature dips to northwest with a 15° dip at ~ 20 to 40 km depth (Figure 5b, black-dashed line). This dipping interface is laterally present up to ~ 100 km from the point B', and it is not clear whether this continues up to the surface because the 2-D GRT migration cannot recover near-surface structure within ~ 20 km from the surface with the current station geometry (Figure 5d). Also, the presence of the Cook Inlet Basin (sediment thickness increasing from 0 to ~ 6 km toward west; Figure 2b) yields complicated first *P* arrivals in the RFs (Figure 5c). If large positive peaks in the RFs at 2.0 to 3.7 s (horizontal distance of ~ 40 km to 0 km, respectively; Figure 5c) are the first positive seismic multiple (PpPs) of the bottom interface of the Cook Inlet Basin, it might be possible that this feature can be mapped as a dipping layer as shown in the migration (Figures 5a and 5b). However, this feature continues farther east near the point close to the western edge of the Yakutat terrane (Figure 5b, black-dashed line). Furthermore, a similar midcrustal interface was previously found based on high-frequency reflected *P* and *S*, and converted *S*-to-*P* (*Sp*) phases in southern Kenai Peninsula from local earthquakes [Stephens et al., 1990], and in marine reflection profiles south of the Kenai Peninsula [Fisher et al., 1983]. In southern Kenai Peninsula, this structure is suggested to be dipping 20 – 30° to the northwest between depths of 12 and 18 km [Stephens et al., 1990] and in offshore Peninsula, 19.6 – 21.8° in similar depths [Fisher et al., 1983]. Onshore seismic results from the TACT experiment [Brocher et al., 1994; Fuis et al., 2008] also showed a series of dipping layers to the north with $\sim 11.5^\circ$ at depths 10–20 km beneath Chugach terrane. Thus, we likely image the Contact Fault or similar terrane-bounding fault as a low-angle thrust.

3.2.3. Finite-Difference Modeling of the Low-Velocity Thrust Zone

In the south beneath the MOOS stations, a thin layer is imaged to be 6 km thick (Figure 4a), and ~ 20 – 40% slower in *S* wave velocity at the top interface of the Yakutat slab (~ 20 – 25 km depth), based on converted amplitudes of *Ps* phase at the top of the thin layer (Figure 4c). However, this thickness of the layer estimated from the migration images might be biased large because of the low-frequency band that is used to filter the data.

We perform finite-difference calculations to precisely constrain the thickness and velocity contrast across the interfaces. The description of the method has been described in previous papers [Kim et al., 2010, 2011]. Synthetic RFs are computed for prescribed velocity and slab geometry models and directly compared to the data (Figures 6, 7, and S9–S11). We select 10 stations, which show good signal-to-noise ratios, atop the thrust zone, and linearly stack individual RFs grouped with different back azimuth (40° bins and all back azimuths) and ray parameter (0.005 s/km bin and all ray parameters) ranges for those stations. The stacked versions become the data traces that will be compared to the synthetics. We then construct models for individual station above the thrust zone to mainly target timings and amplitudes of the primary *Ps* arrivals at the top and bottom of the thrust layer, and bottom of the Yakutat terrane (a negative and double positive pulses arriving at ~ 3 – 7 s) as well as amplitudes and timing of the free-surface multiples such as PpPs and PsPs (and PpSs) of the thrust layer. Since seismic attenuation is not included in the numerical setup, we more focus to fit the arrival time of the multiples, although attenuation effects should be small for < 1 Hz periods and crustal path lengths.

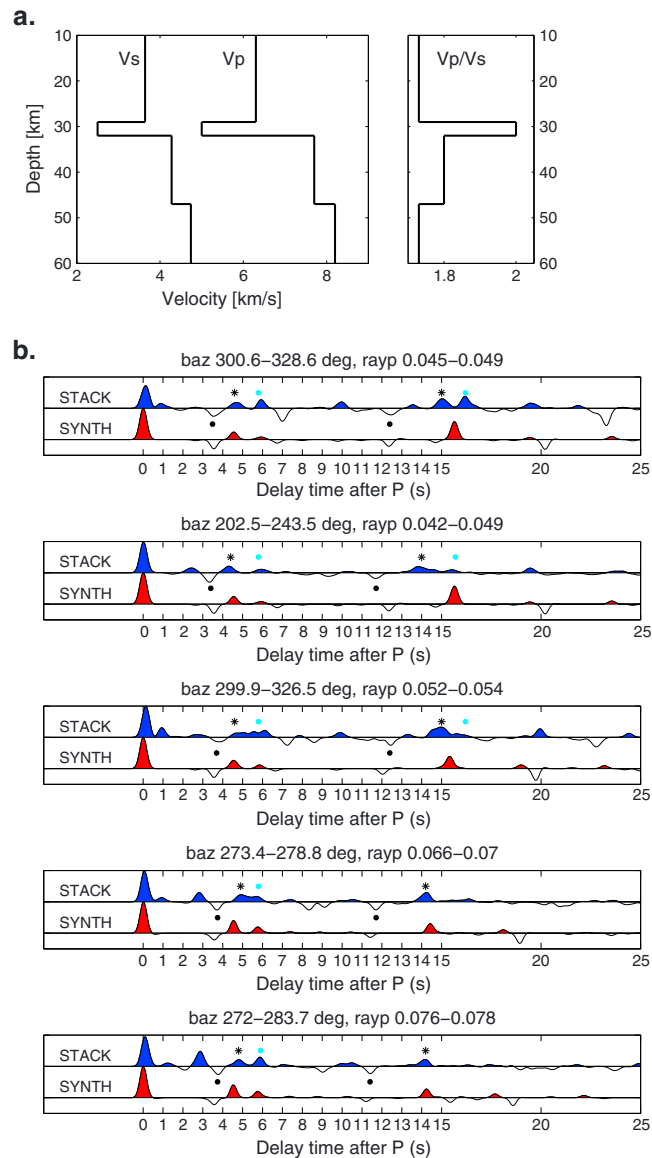


Figure 6. Best-fitting model and RFs for MOOS station DEVL in the thrust zone. (a) Best-fitting model to represent seismic observations in the thrust zone and Yakutat terrane. The thrust zone is a thickness of 3 km, and V_p/V_s of 2.0. (b) Stacked RFs (blue) grouped into different back azimuth bins and ray parameters specified above each panel, compared with the finite-difference synthetics (red) based on the model in Figure 6a. The top and bottom interfaces of the thrust zone are indicated as dots and asterisks, respectively, at 3.5–5 s. The bottom of the Yakutat terrane is indicated as dots in cyan, at 5.7–6 s. We also marked the location of multiples as the same symbols.

To match the negative (red) and double positive (blue) RF pulses (Figure 4c), we require at least two low-velocity layers. The first low-velocity layer (fault zone) includes velocities much lower than normal oceanic crustal velocities, and also those of the lower layer (Yakutat terrane), in order to produce a strong negative arrival below the overlying crust. To obtain candidate models, we fix the following: (1) total thickness of the Yakutat terrane including the top low-velocity fault zone (18 km), (2) P and S velocities for overlying crust (consistent with the values determined by the inversion [Li *et al.*, 2013] (Table 2)), and (3) P and S velocities of the oceanic mantle. Also, we fix the P wave velocities of the fault zone and Yakutat terrane.

Figure 6 shows one candidate model and the comparison between synthetic RFs and data (i.e., stacked RFs for back azimuth (40°) and ray parameter (0.005 s/km) ranges) for station DEVL. Note that the model is

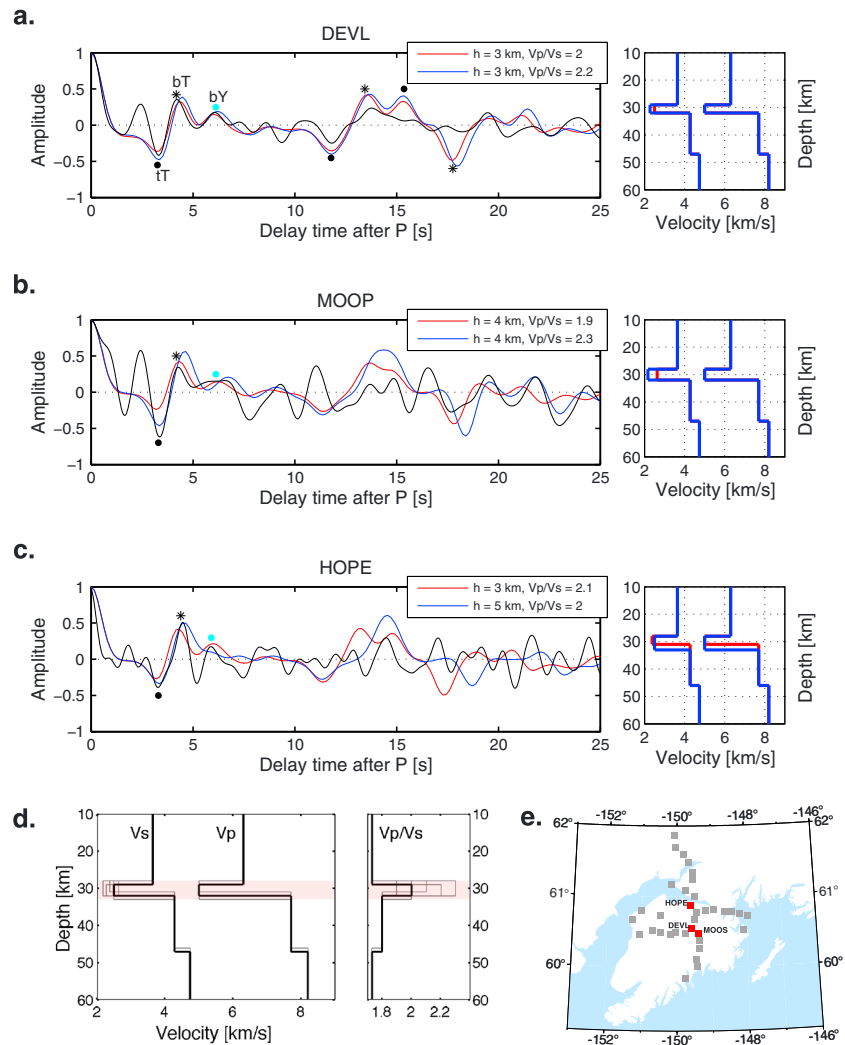


Figure 7. Best-fitting models and RFs for three MOOS stations atop the thrust zone (DEVL, MOOP, and HOPE). (a–c) Synthetic RFs based on various models to constrain the megathrust zone properties for three MOOS stations atop the thrust zone (DEVL (Figure 7a), MOOP (Figure 7b), and HOPE (Figure 7c)). Several models are tested with different thrust layer thickness (h) and V_p/V_s (see supporting information Figures S9–S11). We only plot synthetic traces from lower and upper bounds in both h and V_p/V_s to compare with the single-station stack of the RFs (black line). The top and bottom interfaces of the thrust zone and the bottom of the Yakutat terrane are indicated as “tT,” “bT,” and “bY” with different symbols, respectively. (d) Best-fitting model for the thrust zone. The thickness of the low-velocity thrust layer ranges between 3 and 5 km with V_p/V_s of 1.9–2.3, V_s of 2.17–2.63 km/s, and fixed V_p of 5.0 km/s. The thrust layer is highlighted in light pink overlay. (e) Locations of three seismic stations.

carefully constrained such that the arrival times of the multiples are well predicted at the chosen range of back azimuths and ray parameters.

We first explore candidate models by the approach shown in Figure 6 and then vary thickness (h) and shear wave velocity (or V_p/V_s) of the low-velocity thrust layer to improve the fit between the synthetics and data. Supporting information Figures S9–S11 show the results for three MOOS stations (DEVL, MOOP, and HOPE; Figure 7e) atop of the thrust zone. Supporting information Figures S9a–S11a show the synthetic traces computed for $h = 1$ –6 km with the fixed V_p/V_s for each station. Supporting information Figures S9b–S11b show the synthetics computed for $V_p/V_s = 1.8$ –2.3 with the fixed h . For station DEVL, we observe that the misfit between the synthetics and primary phases (when the delay time in P, $t = \sim 3.5$ –7.0 s) is negligible when $h = 3$ km and $V_p/V_s = 2.0$ –2.2. Also, the fit between synthetics and seismic multiples are qualitatively good after $t = 12$ s. Similarly, we see a similar fitting trend for station MOOP, which is only ~ 10 km from station DEVL (supporting information Figure S10). For station MOOP, we observe that the misfit between the synthetics

and primary phases is reduced when $h = 4$ km and $V_p/V_s = 1.9$ – 2.3 . We note that as the V_p/V_s of the thrust layer increases, the fit between synthetics and data for the multiples enhances whereas the smaller V_p/V_s slightly gives rise to a better fit to the direct conversion from the bottom of the low-velocity zone. Finally, supporting information Figure S11 shows the comparison between the data and synthetics for station HOPE, which is located just north of the 1964 rupture zone (Figure 2). Since seismic noise level is higher, we only consider fits between the data and synthetics for primary phases and only the timing of the first multiple (PpPs), which arrives at $t = 12$ – 15 s. For station HOPE, we observe that the misfit between the synthetics and primary phases is reduced when $h = 3$ – 5 km and $V_p/V_s = 2.0$ – 2.1 (supporting information Figure S11).

Figure 7 only shows (1) synthetics that best fit the data (from the sensitivity test results shown in supporting information Figures S9–S11) for all three stations and (2) corresponding candidate P and S velocity models. The thickness of the low-velocity thrust layer ranges between 3 and 5 km with V_p/V_s of 1.9– 2.3 , V_p of 5.0 km/s, and V_s of 2.17– 2.63 km/s (Figure 7d). This range also accounts for trade-off between layer thickness and velocity variation across the megathrust.

4. Discussion

Seismic images (Figure 4) show a thin low-velocity (S velocity reduction of ~ 20 – 40%) layer with a $< 5^\circ$ dip at 20 to 25 km depths near the Alaskan coast transitioning into a thicker one with a $\sim 20^\circ$ dip and $\sim 20\%$ S velocity reduction down to 130 km depth [Ferris *et al.*, 2003]. The shallower, thin low-velocity layer sits below the continental crust, corresponding to the interplate thrust zone where most of earthquake activity is concentrated, while the deeper layer in the mantle is interpreted as the subducted crust of the Yakutat terrane (Figure 4b).

4.1. Subducted Fault Zone Properties

The most intriguing feature that we image from both 2-D GRT and RFs is the thin (3–5 km) low-velocity layer with ~ 20 – 40% slower in S wave velocity at the top interface of the Yakutat slab (~ 20 – 25 km depth) beneath the overriding North American Plate (Figures 4 and 5). The shear speeds of the layer are estimated to be 2.17– 2.63 km/s, which results in high V_p/V_s of 1.9– 2.3 based on the modeling (Figure 7d). This strong, narrow low-velocity zone may be difficult to explain simply by the velocity difference predicted for plausible subducted oceanic crust lithologies. At 25 km depth or 0.7 GPa, the subducting crust should be 300– 450°C [Abers *et al.*, 2006], and at these conditions, lawsonite blueschist and epidote blueschist should be stable in metabasalts with $V_p = 6.9$ – 7.1 km/s if fully hydrated [Hacker *et al.*, 2003]. Such velocities would be difficult to distinguish from overlying mafic rock, and more intermediate to felsic compositions for the upper plate would have slower wave speeds, so would result in the opposite sign of velocity contrast. Deeper downdip, this assemblage metamorphoses but also passes into the mantle; so 10– 15% velocity contrasts at the top of the subducted crust can be expected, consistent with imaging beneath the north half of A–A' [Ferris *et al.*, 2003; Rondenay *et al.*, 2008, 2010].

The low-velocity anomalies at depth of 20– 25 km within the active subduction megathrust or subduction channel shear zone may reflect properties of incoming, highly sheared, fluid-saturated trench-fill sediments [von Huene *et al.*, 1998; von Huene and Weinrebe, 2012]. In the Gulf of Alaska, there are two major sediment bodies, the Aleutian Trench wedge and the Surveyor Fan, which have contributed significant material to the subduction zone since glacial sedimentation greatly increased in volume at 3 Myr [von Huene and Weinrebe, 2012]. The subduction channels of the accretionary margin commonly contain trench and ocean-basin sediment including clay, silt, and sand [von Huene and Weinrebe, 2012], and the inferred material along the plate interface greatly influences interplate frictional behavior and variable shear strain rates [Fagereng and Sibson, 2010]. Regardless of fluctuations of fluid flow and strain inferred from their images, strain rate and fluid pressure both clearly elevate farther away from the trench axis [von Huene *et al.*, 1998].

Low velocities atop of the subducted oceanic crust, in the Cascadia subduction zone [Abers *et al.*, 2009], a shallow megathrust convergent margin similar to Alaska, and high seismic reflectivity in Nankai Trough subduction megathrust in southwest Japan [Kodaira *et al.*, 2004] and Barbados [Bangs *et al.*, 1999] were previously imaged and also suggested due to a thick metamorphosed sediment layer. The subducting sedimentary column below the plate boundary is expected to have much slower (~ 10 – 30%) velocities than gabbros. Alternatively, or in addition, velocities at the top of the plate could be reduced by fluids in

overpressured channels within or immediately below the plate interface [Audet *et al.*, 2009; Peacock *et al.*, 2011; Hansen *et al.*, 2012]. Elevated fluid pressures would arise from dehydration-produced fluids migrating upward, encountering permeability barriers along the thrust zone. The elevated pore fluid pressure within the subduction channel lowers absolute P and S wave velocities by $\sim 20\%$ and $\sim 30\%$ for $< 4\%$ porosity, respectively [Christensen, 1984], which result in high V_p/V_s . These models do not consider the presence of the underthrusting sediment or metasediment along the megathrust, which can also help explain observed seismic anomalies. Similarly, in Nankai, a zone of high Poisson's ratio was interpreted as elevated pore pressure due to the result of progressive metamorphic dehydration reactions [Kodaira *et al.*, 2004; Kato *et al.*, 2010]. In addition to high fluid pressure, crack anisotropy [Wang *et al.*, 2012] might contribute to observed high V_p/V_s (above 2.2) in the subduction zones, as raypath sampling is often biased [Hacker and Abers, 2012].

In southern Alaska, the subduction of the thick buoyant Yakutat terrane has made the subduction thrust system here have a shallower dip ($\sim 3^\circ$) than typical thrust zones. This 3° dip for the plate interface is about half of the angle that was used in some earthquake rupture models [e.g., Ichinose *et al.*, 2007] to calculate the 1964 seismic moment, because we clearly show that the plate interface follows the top of the Yakutat crust, not its base, as sometimes inferred. This could lead to up to 50% underestimate of the 1964 moment release in such studies, at least for this rupture patch, because of the source excitation function for most radiated wave types is proportional to sine of the dip [Langston and Helmberger, 1975]. Although a full reanalysis of 1964 rupture models is outside the scope of this paper, we expect that the correct moment magnitude is 0.2 higher than the M_w 9.12 estimated by Ichinose *et al.* [2007] were a shallower dip used, more consistent with long-period seismic estimates [Kanamori, 1970].

The slow-slip events occur downdip of the seismogenic zone (Figure 4a, horizontal location > 100 km), which represents the transition zone between completely locked and slipping segments of the plate interface [Ohta *et al.*, 2006]. Farther northwest, both velocities and thickness gradually increase with increasing metamorphic grade in the metasedimentary channel before the slab subducts into the mantle beneath central Alaska.

4.2. Pacific-Yakutat Slab Structure Beneath the Kenai Peninsula

The collision of the Yakutat terrane along the Gulf of Alaska has greatly changed the dynamics between the subducting Pacific and North American plates. Furthermore, the presence of the Yakutat terrane plays an important role in controlling earthquake rupture and was previously suggested to correspond to the region of high displacement during the 1964 earthquake [Christensen and Beck, 1994]. However, the poorly defined Yakutat-Pacific plate geometry beneath the Kenai Peninsula has previously made it hard to tell its relationship to complex rupture process and asperity distribution of the 1964 earthquake.

A striking image based on the mode-converted phases is the western edge of the Yakutat terrane at the horizontal distance of ~ 50 km from the point B (or ~ 120 km from the point B') beneath the Kenai Peninsula (Figure 5). Including the low-velocity megathrust layer, the subducted terrane has a thickness of about 25 km, with its clear bottom interface at ~ 50 km depth (Figure 5). This thickness is consistent with offshore and onshore observations by Worthington *et al.* [2012] and Ferris *et al.* [2003], respectively.

Major change in thickness and dip of the imaged downgoing plates beneath the Kenai (Figure 5) coincide with drastic changes in locking at the plate interface as revealed by GPS, suggesting a causal link. Dense GPS data previously constrained the location of the edge of the locked zone (or asperity, the area of large moment release) to lie beneath the eastern end of the Kenai Peninsula [Zweck *et al.*, 2002; Suito and Freymueller, 2009]. The westernmost extent of such geodetically determined locked patch very closely corresponds to the abrupt edge of the Yakutat imaged along B-B' (Figure 5a). Also, the Yakutat slab edge lies ~ 15 km east of the northwest extent of 1964 rupture (Figures 2b and 5d) and thus provides a direct evidence that the main Prince William Sound asperity is related to the terrane subduction. This region also corresponds to the megathrust zone that is suggested to involve fluid-rich, highly sheared sediments atop of the subducted Yakutat terrane. As discussed earlier, such subducting (input) materials impact megathrust properties in the subduction system.

5. Conclusions

The geodynamics of the southern Alaskan convergence margin is predominantly controlled by the collision of the Yakutat terrane with North America. Utilizing high-quality seismograms from dense

broadband array stations (MOOS and BEAR), we provide two crossing 2-D images of subduction beneath south-central Alaska. They show (1) a shallowly dipping plate interface from the coast to 450 km inland and plate boundary processes associated with the Yakutat terrane in Alaskan margin, and (2) Pacific Plate subduction beneath Cook Inlet Basin and western edge of the Yakutat terrane. A thin, $<5^\circ$ dipping low-velocity layer is imaged at depths 25–40 km in the two profiles, with velocities 20–40% lower than surroundings. This low-velocity channel reflects the plate interface material including marine sediment transported into the subduction system along the thrust interface, perhaps enhanced by high pore fluid pressure. The layer thickness varies between 3 and 5 km with shear wave velocity of ~ 2.1 – 2.6 km/s (and V_p/V_s exceeding 2.0). This layer steepens to dips exceeding 20° and appears to become thickened in central Alaska, along line A–A', but the thicker layer may represent the entire subducting crust not just its top. At 70–130 km depth, the low-velocity subducting Yakutat crust is 15–20 km thick, which agrees with previously published results. The apparent thickening is probably an artifact of the absence of the very low velocity subduction channel once the plate surface is >50 km deep, so that the top and bottom of the subducted Yakutat crust can be seen. At shallow depths more careful analysis of receiver functions shows the Yakutat Moho is present there as well, and it can be seen in the B–B' cross line clearly. The migration image along the Pacific Plate downdip direction shows (1) the Pacific Plate subduction with a 20° dip down to a depth of 55 km beneath Cook Inlet Basin, and (2) the abrupt western edge of the Yakutat terrane, which directly aligns with the western end of the geodetically locked zone. This provides evidence that the main Prince William Sound asperity is related to the Yakutat terrane subduction.

Acknowledgments

This study was supported by National Science Foundation grant EAR-0814235. This work was also funded by the Korea Meteorological Administration Research and Development Program under grant CATER-2013-8010. We thank F. Waldhauser (LDEO, Columbia University) for the help on relocating local earthquakes. Many figures are made using GMT [Wessel and Smith, 1991]. Finally, we thank the Associate Editor, Pascal Audet, and one anonymous reviewer for their helpful comments.

References

- Abers, G. A., P. E. van Keken, E. A. Kneller, A. Ferris, and J. C. Stachnik (2006), The thermal structure of subduction zones constrained by seismic imaging: Implications for slab dehydration and wedge flow, *Earth Planet. Sci. Lett.*, *241*(3–4), 387–397.
- Abers, G. A. (2008), Orogenesis from subducting thick crust and evidence from Alaska, in *Active Tectonics and Seismic Potential of Alaska*, AGU Monograph, vol. 179, edited by P. Haeussler et al., pp. 337–349, AGU, Washington, D. C.
- Abers, G. A., L. S. MacKenzie, S. Rondenay, Z. Zhang, A. G. Wech, and K. G. Creager (2009), Imaging the source region of Cascadia tremor and intermediate-depth earthquakes, *Geology*, *37*(12), 1119–122, doi:10.1130/G30143A.1.
- Audet, P., M. G. Bostock, N. I. Christensen, and S. M. Peacock (2009), Seismic evidence for overpressured subducted oceanic crust and megathrust fault sealing, *Nature*, *457*, 76–78, doi:10.1038/nature07650.
- Bangs, N. L., T. H. Shipley, J. C. Moore, and G. F. Moore (1999), Fluid accumulation and channeling along the northern Barbados Ridge decollement thrust, *J. Geophys. Res.*, *104*, 20,399–320,414, doi:10.1029/1999JB900133.
- Bostock, M. G., and S. Rondenay (1999), Migration of scattered teleseismic body waves, *Geophys. J. Int.*, *137*, 732–746.
- Bostock, M. G., S. Rondenay, and J. Shragge (2001), Multiparameter two-dimensional inversion of scattered teleseismic body waves, 1, Theory for oblique incidence, *J. Geophys. Res.*, *106*, 30,771–30,782.
- Brocher, T. M., G. S. Fuis, M. A. Fisher, G. Plafker, and M. J. Moses (1994), Mapping the megathrust beneath the northern Gulf of Alaska using wide-angle seismic data, *J. Geophys. Res.*, *99*, 11,663–11,685.
- Bruhn, R. L., T. L. Pavlis, G. Plafker, and L. Serpa (2004), Deformation during terrane accretion in the Saint Elias orogen, Alaska, *Geol. Soc. Am. Bull.*, *116*(7/8), 771–787, doi:10.1130/B25182.1.
- Bruns, T. R. (1983), Model for the origin of the Yakutat block, an accreting terrane in the northern Gulf of Alaska, *Geology*, *11*, 718–721.
- Christensen, D. H., and S. L. Beck (1994), The rupture process and tectonic implications of the Great 1964 Prince William Sound Earthquake, *Pure Appl. Geophys.*, *142*(1), 29–53.
- Christensen, N. I. (1984), Pore pressure and oceanic crustal seismic structure, *Geophys. J. R. Astron. Soc.*, *79*, 411–423.
- Christeson, G. L., S. P. S. Gulick, H. J. A. van Avendonk, L. L. Worthington, R. S. Reece, and T. L. Pavlis (2010), The Yakutat terrane: Dramatic change in crustal thickness across the Transition Fault, Alaska, *Geology*, *38*(10), 895–898, doi:10.1130/G31170.1.
- Christeson, G. L., H. J. A. van Avendonk, S. P. S. Gulick, R. S. Reece, G. L. Pavlis, and T. L. Pavlis (2013), Moho interface beneath Yakutat terrane, southern Alaska, *J. Geophys. Res. Solid Earth*, *118*, 5084–5097, doi:10.1002/jgrb.50361.
- Creager, K. C., and T. M. Boyd (1991), The geometry of Aleutian subduction: Three-dimensional kinematic flow model, *J. Geophys. Res.*, *96*, 2293–2307, doi:10.1029/90JB01918.
- Doser, D. I., and A. M. Veilleux (2009), A comprehensive study of the seismicity of the Kenai Peninsula–Cook Inlet Region, South-Central Alaska, *Bull. Seismol. Soc. Am.*, *99*(4), 2208–2222, doi:10.1785/0120080251.
- Eberhart-Phillips, D., D. H. Christensen, T. M. Brocher, R. Hansen, N. A. Ruppert, P. J. Haeussler, and G. A. Abers (2006), Imaging the transition from Aleutian subduction to Yakutat collision in central Alaska, with local earthquakes and active source data, *J. Geophys. Res.*, *111*, B11303, doi:10.1029/2005JB004240.
- Elliott, J. L., C. F. Larson, J. T. Freymueller, and R. J. Motyka (2010), Tectonic block motion and glacial isostatic adjustment in southeast Alaska and adjacent Canada constrained by GPS measurements, *J. Geophys. Res.*, *115*, B09407, doi:10.1029/2009JB007139.
- Elliott, J., J. T. Freymueller, and C. F. Larsen (2013), Active tectonics of the St. Elias Orogen, Alaska, observed with GPS measurements, *J. Geophys. Res. Solid Earth*, *118*, 5625–5642, doi:10.1002/jgrb.50341, in press.
- Fagereng, A., and R. H. Sibson (2010), Melange rheology and seismic style, *Geology*, *38*, 751–754, doi:10.1130/G30868.1.
- Ferris, A., G. A. Abers, D. H. Christensen, and E. Veenstra (2003), High resolution image of the subducted Pacific (?) plate beneath central Alaska, 50–150 km depth, *Earth Planet. Sci. Lett.*, *214*, 575–588, doi:10.1016/S0012-821X(03)00403-5.
- Freymueller, J. F., H. Woodard, S. C. Cohen, R. Cross, J. Elliott, C. F. Larsen, S. Hreinsdottir and C. Zweck (2008), Active deformation processes in Alaska, based on 15 years of GPS measurements, in *Active Tectonics and Seismic Potential of Alaska*, Geophysical Monograph Series, vol. 179, edited by J. T. Freymueller, pp. 1–42, AGU, Washington, D. C., doi:10.1029/179GM02.

- Fisher, M. A., R. von Huene, G. L. Smith, and T. R. Bruns (1983), Possible seismic reflections from the downgoing Pacific Plate, 275 km arcward from the Eastern Aleutian Trench, *J. Geophys. Res.*, **88**, 5835–5849.
- Fuis, G. S., et al. (2008), Trans-Alaska Crustal Transect and continental evolution involving subduction underplating and synchronous foreland thrusting, *Geology*, **36**(3), 267–270, doi:10.1130/G24257A.1.
- Furumoto, A. S. (1964), Analysis of Rayleigh wave, part II, in *Source Mechanism Study of the Alaska Earthquake and Tsunami of March 27, 1964*, Rep. HIG-65-17, pp. 31–42, Univ. of Hawaii, Inst. of Geophys., Honolulu, Haw.
- Gutscher, M.-A., W. Spakman, H. Bijwaard, and E. R. Engdahl (2000), Geodynamics of flat subduction: Seismicity and tomographic constraints from the Andean margin, *Tectonics*, **19**, 814–833, doi:10.1029/1999TC001152.
- Hacker, B. R., G. A. Abers, and S. M. Peacock (2003), Subduction factory 1. Theoretical mineralogy, densities, seismic wave speeds, and H₂O contents, *J. Geophys. Res.*, **108**(B1), 2029, doi:10.1029/2001JB001127.
- Hacker, B. R., and G. A. Abers (2012), Subduction factory 5: Unusually low Poisson's ratios in subduction zones from elastic anisotropy of peridotite, *J. Geophys. Res.*, **117**, B06308, doi:10.1029/2012JB009187.
- Hansen, R. T., M. G. Bostock, and N. I. Christensen (2012), Nature of the low velocity zone in Cascadia from receiver function waveform inversion, *Earth Planet. Sci. Lett.*, **337**–338, 25–38.
- Ichinose, G., P. Somerville, H. K. Thio, R. Graves, and D. O'Connell (2007), Rupture process of the 1964 Prince William Sound, Alaska, earthquake from the combined inversion of seismic, tsunami, and geodetic data, *J. Geophys. Res.*, **112**, B07306, doi:10.1029/2006JB004728.
- Kanamori, H. (1970), The Alaska Earthquake of 1964: Radiation of long-period surface waves and source mechanism, *J. Geophys. Res.*, **75**, 5029–5040, doi:10.1029/JB075i026p05029.
- Kato, A., et al. (2010), Variations of fluid pressure within the subducting oceanic crust and slow earthquakes, *Geophys. Res. Lett.*, **37**, L14310, doi:10.1029/2010GL043723.
- Kim, Y., R. W. Clayton, and J. M. Jackson (2010), The geometry and seismic properties of the subducting Cocos plate in central Mexico, *J. Geophys. Res.*, **115**, B06310, doi:10.1029/2009JB006942.
- Kim, Y., R. W. Clayton, and F. Keppie (2011), Evidence of a collision between the Yucatan Block and Mexico in the Miocene, *Geophys. J. Int.*, **187**, 989–1000, doi:10.1111/j.1365-246X.2011.05191.x.
- Kim, Y., R. W. Clayton, P. Asimow, and J. M. Jackson (2013), Generation of talc in the mantle wedge and its role on the subduction dynamics in central Mexico, *Earth Planet. Sci. Lett.*, **384**, 81–87, doi:10.1016/j.epsl.2013.10.006.
- Kodaira, S., T. Iidaka, A. Kato, J. Park, T. Iwasaki, and Y. Kaneda (2004), High pore fluid pressure may cause silent slip in the Nankai Trough, *Science*, **304**, 1295–1298, doi:10.1126/science.1096535.
- Langston, C. A., and D. V. Helmberger (1975), A procedure for modelling shallow dislocation sources, *Geophys. J. R. Astron. Soc.*, **42**, 117–130.
- Langston, C. A. (1979), Structure under Mount Rainier, Washington, inferred from teleseismic body waves, *J. Geophys. Res.*, **84**, 4749–4762, doi:10.1029/JB084iB09p04749.
- Lay, T., and S. Bilek (2007), Anomalous earthquake ruptures at shallow depths on subduction zone megathrusts, in *The Seismogenic Zone of Subduction Thrust Faults*, edited by T. H. Dixon and J. C. Moore, pp. 476–511, Columbia Univ. Press, New York.
- Lay, T., H. Kanamori, C. J. Ammon, K. D. Koper, A. R. Hutko, L. Ye, H. Yue, and T. M. Rushing (2012), Depth-varying rupture properties of subduction zone megathrust faults, *J. Geophys. Res.*, **117**, B04311, doi:10.1029/2011JB009133.
- Li, J., G. A. Abers, Y. Kim, and D. Christensen (2013), Alaska megathrust 1: Seismicity 43 years after the great 1964 Alaska megathrust earthquake, *J. Geophys. Res. Solid Earth*, **118**, 4861–4871, doi:10.1002/jgrb.50358.
- Ligorria, J. P., and C. J. Ammon (1999), Iterative deconvolution and receiver function estimation, *Bull. Seismol. Soc. Am.*, **89**, 19–36.
- MacKenzie, L. S., G. A. Abers, S. Rondenay, and K. M. Fischer (2010), Imaging a steeply dipping subducting slab in Southern Central America, *Earth Planet. Sci. Lett.*, **296**, 3–4, doi:10.1016/j.epsl.2010.05.033.
- Ohta, Y., J. T. Freymueller, S. Hreinsdottir, and H. Suito (2006), A large slow slip event and the depth of the seismogenic zone in the south central Alaska subduction zone, *Earth Planet. Sci. Lett.*, **247**, 108–116, doi:10.1016/j.epsl.2006.05.013.
- Peacock, S. M., N. I. Christensen, M. G. Bostock, and P. Audet (2011), High pore pressures and porosity at 35 km depth in the Cascadia subduction zone, *Geology*, **39**(5), 471–474, doi:10.1130/G31649.1.
- Pearce, F. D., S. Rondenay, M. Sachpazi, M. Charalampakis, and L. H. Royden (2012), Seismic investigation of the transition from continental to oceanic subduction along the western Hellenic Subduction Zone, *J. Geophys. Res.*, doi:10.1029/2011JB009023, in review.
- Peterson, C. L., and D. H. Christensen (2009), Possible relationship between nonvolcanic tremor and the 1998–2001 slow slip event, south central Alaska, *J. Geophys. Res.*, **114**, B06302, doi:10.1029/2008JB006096.
- Plafker, G., J. C. Moore, and G. R. Winkler (1994), Geology of the southern Alaska margin, in *The Geology of Alaska*, vol. G1, edited by G. Plafker and H. C. Berg, pp. 384–449, Geol. Soc. Am. Bull., Boulder, CO.
- Ratchkovski, N. A., and R. A. Hansen (2002), New evidence for segmentation of the Alaska subduction zone, *Bull. Seismol. Soc. Am.*, **92**(5), 1754–1765.
- Rondenay, S., M. G. Bostock, and J. Shragge (2001), Multiparameter two-dimensional inversion of scattered teleseismic body waves, 3. Application to the Cascadia 1993 data set, *J. Geophys. Res.*, **106**, 30,795–30,807.
- Rondenay, S., M. G. Bostock, and K. M. Fischer (2005), Multichannel inversion of scattered teleseismic body waves: Practical considerations and applicability, in *Seismic Earth: Array Analysis of Broadband Seismograms*, AGU Geophysical Monograph Series, vol. 157, edited by A. Levander and G. Nolet, pp. 187–203, AGU, Washington, D. C.
- Rondenay, S., G. A. Abers, and P. E. van Keken (2008), Seismic imaging of subduction zone metamorphism, *Geology*, **34**, 275–278, doi:10.1130/G24112A.1.
- Rondenay, S. (2009), Upper mantle imaging with array recordings of converted and scattered teleseismic waves, *Surv. Geophys.*, **30**, 377–405, doi:10.1007/s10712-009-9071-5.
- Rondenay, S., L. G. J. Montési, and G. A. Abers (2010), New geophysical insight into the origin of the Denali volcanic gap, *Geophys. J. Int.*, **182**, 613–630, doi:10.1111/j.1365-246X.2010.04659.x.
- Rossi, G., G. A. Abers, and S. Rondenay (2006), Unusual mantle Poisson's ratio, subduction, and crustal structure in central Alaska, *J. Geophys. Res.*, **111**, B09311, doi:10.1029/2005JB003956.
- Shellenbaum, D. P., L. S. Gregersen, and P. R. Delaney (2010), Top Mesozoic unconformity depth map of the Cook Inlet Basin, Alaska, Alaska Division of Geological & Geophysical Surveys Report of Investigation 2010-2, 1 sheet, scale 1:500,000.
- Song, T.-R., and Y. Kim (2012a), Localized seismic anisotropy associated with slow earthquakes beneath southern Mexico, *Geophys. Res. Lett.*, **39**, L09308, doi:10.1029/2012GL051324.
- Song, T.-R., and Y. Kim (2012b), Anisotropic uppermost mantle in young subducted slab underplating central Mexico, *Nat. Geosci.*, **5**, 55–59, doi:10.1038/ngeo1342.
- Stephens, C. D., R. A. Page, and J. C. Lahr (1990), Reflected and mode-converted seismic waves within the shallow Aleutian subduction zone, southern Kenai Peninsula, Alaska, *J. Geophys. Res.*, **95**, 6883–6897.

- Suito, H., and J. T. Freymueller (2009), A viscoelastic and afterslip postseismic deformation model for the 1964 Alaska earthquake, *J. Geophys. Res.*, *114*, B11404, doi:10.1029/2008JB005954.
- Sykes, L. R. (1971), Aftershock zones of great earthquakes, seismicity gaps, and earthquake prediction for Alaska and the Aleutians, *J. Geophys. Res.*, *76*, 8021–8041.
- Veenstra, E., D. H. Christensen, G. A. Abers, and A. Ferris (2006), Crustal thickness variation in south-central Alaska, *Geology*, *34*(9), 781–784, doi:10.1130/G22615.1.
- Von Huene, R., D. Klaeschen, M. Gutscher, and J. Fruehn (1998), Mass and fluid flux during accretion at the Alaskan margin, *Geol. Soc. Am. Bull.*, *110*(4), 468–482.
- von Huene, R. J. J. M., and W. Weinrebe (2012), Subducting plate geology in three great earthquake ruptures of the western Alaska margin, Kodiak to Unimak, *Geosphere*, *8*(3), 628–644, doi:10.1130/GES00715.1.
- Wang, X.-Q., A. Schubnel, J. Fortin, E. C. David, Y. Gueguen, and H.-K. Ge (2012), High V_p/V_s ratio: Saturated cracks or anisotropy effects?, *Geophys. Res. Lett.*, *39*, L11307, doi:10.1029/2012GL051742.
- Wessel, P., and W. H. F. Smith (1991), Free software helps map and display data, *EOS Trans. AGU*, *72*, 441.
- Worthington, L. L., H. J. A. Van Avendonk, S. P. S. Gulick, G. L. Christeson, and T. L. Pavlis (2012), Crustal structure of the Yakutat terrane and the evolution of subduction and collision in southern Alaska, *J. Geophys. Res.*, *117*, B01102, doi:10.1029/2011JB008493.
- Zhu, L., and H. Kanamori (2000), Moho depth variation in southern California from teleseismic receiver functions, *J. Geophys. Res.*, *105*, 2969–2980.
- Zweck, C., J. T. Freymueller, and S. C. Cohen (2002), Three-dimensional elastic dislocation modeling of the postseismic response to the 1964 Alaska earthquake, *J. Geophys. Res.*, *107*(B4), 2064, doi:10.1029/2001JB000409.